Modelling and simulation of the freeze casting process with the phase-field method

Marco Seiz[a,*], Britta Nestler[a,b]

[a] *Institute of Applied Materials, Karlsruhe Institute of Technology, Straße am Forum 7, 76131 Karlsruhe, Germany*
[b] *Institute of Digital Materials, Hochschule Karlsruhe Technik und Wirtschaft, Moltkestr. 30, 76131 Karlsruhe, Germany*

Abstract

The freeze casting process is a novel manufacturing method for both near net-shape parts as well as directed porous structures as employed by filters and implants. Depending on the choice of liquid and processing conditions a very wide range of pore shapes and sizes can be achieved. In order to predict the resulting microstructure, a phase-field model is developed on the basis of the grand potential formalism. The model and its parametrization approximate the freeze-casting process of water by linking its thermodynamics with established theory. Directional solidification simulations with varying suspension concentrations, velocities and temperature gradients are carried out. From these, microstructural lengths are determined and linked with the processing parameters, so as to derive linkages between the microstructure and the processing conditions.

Keywords: solidification, freeze casting, phase-field, simulation

1. Introduction

Freeze casting is a novel manufacturing approach with applications including near net-shape casting [1] and generation of directed porous structures for filters [2] and implants [3–5]. The process is based on the freezing of a colloidal suspension, i.e. insoluble particles are suspended in a liquid, which is

*Corresponding author
Email address: marco.seiz@kit.edu (Marco Seiz)

then frozen directionally. Depending on the liquid and its composition, many different microstructures can be obtained, ranging from lamellar structures for water [6] to faceted matrix-rod structures for tert-butyl alcohol [7]. Besides the morphology of the microstructure, its lengths in terms of e.g. lamellar distances or widths, can be adjusted by varying process parameters such as the solidification velocity, the temperature gradient or the solids loading of the suspension. Since material properties are linked to the microstructure morphology and its lengths, this allows the production of materials with tailored properties, given that one can predict the microstructure based on given processing conditions.

The phase-field method has garnered much attention in the last decades in determining such linkages between processing conditions and the resulting microstructure. In the context of solidification, it was shown to quantitatively model dendritic growth [8, 9] as well as eutectic growth [10]. Specifically for freeze casting, Huang et al. [11] have published a phase-field model based on the free-energy formulation of Echebarria et al. [12] coupled with a particle concentration field and an analytical temperature field to describe the freeze-casting process. In the work of Huang et al., the individual particles within the suspension have already been coarse-grained over by employing a particle concentration field instead of tracking individual particles. Besides the reasons stated in their work, one must consider the computational expense: Typical freeze-cast structures show wavelengths from a few microns to hundreds of microns, whereas the particles which form these structures may be on the order of hundreds of nanometers. Resolving these particles within the structures they form is prohibitively expensive — but if the particles are coarse grained over, only the structure itself needs to be resolved.

Prior research by Peppin et al. [13] described the freeze casting process as a kind of osmosis, in which the suspended particles are entirely rejected by the advancing ice front. By doing so Peppin et al. were able to find an expression for the chemical potential of the suspension as well as the liquidus curve as a function of solids loading and temperature. In this paper, the expressions derived by Peppin et al. are used to construct free energies representing the freeze

casting process. Furthermore, qualitative expressions for the interfacial as well as kinetic anisotropy of the ice-water interface are presented. Finally, directional solidification simulations employing the above are conducted and a linkage between processing condition and resulting microstructure is established.

2. Phase-field model

The employed phase-field model is based on the work of Choudhury [14]. A grand potential type of formalism is chosen since it decouples interfacial properties from the bulk energies as described in [15]. The original model is composed for multicomponent and multiphase systems. In the present paper the model is restricted to two phases ($N = 2$) and two components ($K = 2$) which simplifies the mathematical equations.

The phase-field equation is based on a variational derivative of a functional describing the contributions of interfacial and bulk energies. Performing the variational derivative and using the Allen-Cahn Ansatz for the time evolution yields

$$\begin{aligned}\tau(\phi,\nabla\phi)\varepsilon\frac{\partial\phi_\alpha}{\partial t} = -\Bigg(&\varepsilon\left(\frac{\partial a(\phi,\nabla\phi)}{\partial\phi_\alpha} - \nabla\cdot\frac{\partial a(\phi,\nabla\phi)}{\partial\nabla\phi_\alpha}\right)\\ &+\frac{1}{\varepsilon}\frac{\partial w(\phi)}{\partial\phi_\alpha} + \frac{\partial\psi(T,\mu,\phi)}{\partial\phi_\alpha} - \Lambda\Bigg),\end{aligned} \tag{1}$$

with a, w describing the contribution of interfacial energy and ψ that of the bulk energy. $\tau(\phi,\nabla\phi)$ is the kinetic coefficient, which fixes a timescale for the phase-field evolution. ε is related to the interface width W by $W \approx 2.5\varepsilon$. The term Λ is a Lagrange multiplier ensuring the constraint $\sum_{\alpha=1}^{N}\frac{\partial\phi_\alpha}{\partial t} = 0$. The grand potential density $\psi = \sum_{\alpha=1}^{N} h_\alpha(\phi)\psi_\alpha$ is the driving force for phase transformation. It is related to the phase-specific Gibbs free energy density by $\psi_\alpha = G_\alpha - \mu c$. Close to equilibrium, the Gibbs free energy can be approximated as a parabolic function of concentration, or volumetric solids loading, c

$$G_\alpha(c,T) = A_\alpha(T)c^2 + B_\alpha(T)c + C_\alpha(T) \tag{2}$$

with functions $A_\alpha, B_\alpha, C_\alpha$ which are parabolic functions of temperature. In the next section, the Gibbs energies will be determined in such a way that the freeze-casting process is approximated. The interpolation function for the grand potential density is formulated as $h_\alpha(\phi) = \frac{\phi_\alpha^2}{\sum_{\beta=1}^{N} \phi_\beta^2}$ following [16].

The gradient energy density a is expressed as

$$a(\phi, \nabla\phi) = \gamma_{\alpha\beta} a_{cap}^2(q_{\alpha\beta}) |q_{\alpha\beta}|^2 \tag{3}$$

with $\gamma_{\alpha\beta}$ being the isotropic interface energy for the α-β interface and $q_{\alpha\beta} = \phi_\alpha \nabla\phi_\beta - \phi_\beta \nabla\phi_\alpha$ being the generalized gradient vector. The term a_{cap} describes the anisotropy of the gradient energy density and will be further detailed in the next section. An equal form is employed for the kinetic coefficient τ

$$\tau(\phi, \nabla\phi) = \tau_{\alpha\beta} a_{kin}^2(q_{\alpha\beta}) |q_{\alpha\beta}|^2. \tag{4}$$

The obstacle potential w is employed and simplified for two phases

$$\begin{aligned} w(\phi) &= \frac{16}{\pi^2} \sum_{\substack{\alpha=1,\beta=1 \\ \beta\neq\alpha}}^{N,N} \gamma_{\alpha\beta}\phi_\alpha\phi_\beta + TPT \\ &= \frac{16}{\pi^2} \gamma_{\alpha\beta}\phi_\alpha\phi_\beta \end{aligned} \tag{5}$$

with the three phase term (TPT) vanishing since only two phases are considered. An obstacle type of potential is chosen for computational efficiency, as the phase-field need only be updated in the interfacial regions.

The phase-field equation is coupled with the chemical potential evolution equation

$$\begin{aligned} \frac{\partial\mu}{\partial t} = &\left[\sum_{\alpha=1}^{N} h_\alpha(\phi) \left(\frac{\partial \mathbf{c}_\alpha(\mu, T)}{\partial\mu}\right)\right]^{-1} \\ &\left[\left(\nabla \cdot \Big(\mathbf{M}(\phi, \mu, T)\nabla\mu - \mathbf{J}_{at}(\phi, \mu, T) + \xi(\mathbf{r}, t)\Big)\right.\right. \\ &\left.\left. - \sum_{\alpha=1}^{N} \mathbf{c}_\alpha(\mu, T) \frac{\partial h_\alpha(\phi)}{\partial t} - \sum_{\alpha=1}^{N} h_\alpha(\phi) \left(\frac{\partial \mathbf{c}_\alpha(\mu, T)}{\partial T}\right) \frac{\partial T}{\partial t}\right]. \end{aligned} \tag{6}$$

The first term on the right-hand side is a generalized susceptibility [17]. This is multiplied by the change of concentration due to Fickian fluxes, an antitrapping current to prevent artificially enhanced solute trapping [9] as well as the change of concentration due to a change in the coupled fields of phase-field ϕ and temperature T. The mobility $\mathbf{M}$ is defined as $\mathbf{M} = \sum_{\alpha}^{N} \phi_\alpha \frac{\partial \mathbf{c}_\alpha}{\partial \mu} \mathbf{D}_\alpha$ with the diffusivity $\mathbf{D}_\alpha$ of each component in the phase α. $\xi(\mathbf{r}, t)$ is a fluctuation term for inducing instabilities. A small, non-vanishing diffusivity is applied in the solid in order to smooth out fluctuations in the concentration field after the phase-field has already passed.

Finally, an external temperature gradient is applied to the system

$$T(x, t) = T_s + G(x - vt) \tag{7}$$

with T_s being the starting temperature, G the temperature gradient, v the velocity thereof, t the simulation time and the coordinate x pointing in the growth direction.

Equations (1), (6) and (7) are solved with the massive parallel PACE3D framework ("Parallel Algorithms for Crystal Evolution in 3D")[18]. Within the framework the equations are discretized on a uniform grid with finite differences being used to compute derivatives. The time integration is done with the explicit Euler method. Parallelization is achieved by using the Message Passing Interface and spatial domain decomposition. The temperature given by eq. (7) is calculated for each grid point and timestep.

3. Parametrization of freeze casting

The key in linking the phase-field evolution to a specific material lies in its parametrization in terms of energies and kinetics. In this paper, the focus will be on the energetic part, specifically the complex anisotropy of the ice-water interface and the grand potential density of colloidal suspensions. The energetic contribution consists of the interfacial and the bulk energies. Many experimental studies ([19–21] and references in [22]) exist for the determination of the

interfacial energy between ice and water, with values ranging from $25\,\mathrm{mJ/m^2}$ to $45\,\mathrm{mJ/m^2}$ — for the purpose of simplicity a value of $30\,\mathrm{mJ/m^2}$ is assumed, which is close to the data of Hardy [21]. This value describes the *isotropic* behavior, but ice is an anisotropic material. For its capillary anisotropy the function a_{cap} is expanded into a sum of spherical harmonics Y_{lm}:

$$\begin{aligned} a_{cap}(\vec{q}_{\alpha\beta}) &= \sum_{l,m} \epsilon_{lm} Y_{lm}(\vec{q}_{\alpha\beta}) \\ &= 1 + \epsilon_{4,0}^{cap} Y_{4,0}(\vec{q}_{\alpha\beta}) + \epsilon_{6,6}^{cap} Y_{6,6}(\vec{q}_{\alpha\beta}), \end{aligned} \tag{8}$$

which yields a smooth, weak hexagonal capillary anisotropy with the coefficients $\epsilon_{4,0}^{cap} = -0.045, \epsilon_{6,6}^{cap} = 0.0015$. This choice is due to relatively small difference in interfacial energies according to [23–25][26, p. 440]. Furthermore, [27] showed that below a critical undercooling the interface is smooth, implying that the typical hexagonal shape is due to kinetic effects rather than capillary ones, hence the weak capillary anisotropy. This, together with the different kinetics along the basal and prismal planes [28], is reproduced via the kinetic anisotropy function a_{kin}:

$$a_{kin}(\vec{q}_{\alpha\beta}) = 1 + \epsilon_{2,0}^{kin} Y_{2,0}(\vec{q}_{\alpha\beta}) + \epsilon_{4,0}^{kin} Y_{4,0}(\vec{q}_{\alpha\beta}) + \epsilon_{6,6}^{kin} Y_{6,6}(\vec{q}_{\alpha\beta}) \tag{9}$$

with coefficients $\epsilon_{2,0}^{kin} = -0.66, \epsilon_{4,0}^{kin} = -0.34, \epsilon_{6,6}^{kin} = 0.15$ yielding a strong hexagonal anisotropy in the basal plane with a marked reduction in growth kinetics normal to the basal plane. The base value $\tau_{\alpha\beta}$ is chosen such that diffusion-controlled growth is ensured.

The bulk energetic contribution enters the phase-field model from the previous section by the grand potential differences, which are related to differences in Gibbs free energy. For pure ice and water, the International Association for the Properties of Water and Steam (IAPWS) formulations [29] provide extensive thermodynamic information, including the enthalpy and Gibbs energy as a function of temperature. These allow the fitting of the concentration-independent term $C_\alpha(T)$ in eq. (2) for ice and water. The enthalpy of each phase α can be

derived from the Gibbs energy by

$$H_\alpha = G_\alpha - (\frac{\partial G_\alpha}{\partial T})_{P,c}. \tag{10}$$

Both the enthalpy and Gibbs free energy are fitted against data provided by the IAPWS formulations with the `LSSolve` function of Maple. Back-calculating from the fitted enthalpy for the latent heat showed excellent agreement with a relative error of 1.3 %.

However, to the authors' knowledge there is no experimental data for the enthalpy or Gibbs free energy in aqueous colloidal suspensions. Hence the model of Peppin et al. [13, 30] is utilized in order to extend the description from pure water and ice to aqueous suspensions, specifically aqueous suspensions of bentonite. The liquidus curve

$$T_l(c) = T_m(1 + mc\frac{1 + a_1c + a_2c^2 + a_3c^3 + a_4c^4}{1 - c/c_p})^{-1}, \tag{11}$$

with the coefficients of [30] and $c_p = 0.64$ being the random dense-packing density (RDP), describes the temperature below which a coarse-grained suspension begins to separate into a solid ice phase and the remaining suspension. The factor $m = \frac{k_b T_m}{V_p \rho_f L_f}$ with the Boltzmann constant k_b, the melting temperature of the pure substance T_m, the volume of an individual particle V_p, the fluid density ρ_f and its melting enthalpy L_f incorporates the effect of differently sized particles. The origin of the dependence on the particle volume is its inclusion in the osmotic pressure of a suspension of hard spheres, which is employed by Peppin et al. [13] to derive eq. (11). The particles are assumed to be spherical and thus $V_p = \frac{4}{3}\pi r^3$ with r being the radius of an individual particle. From this it can be seen that the liquidus curve in the model of Peppin et al. depends significantly on the radius of the suspended particles, with smaller particles resulting in steeper liquidus curves.

The connection between the liquidus curve and the chemical equilibrium conditions is exploited in order to establish a least-squares problem for the functions $A_\alpha(T), B_\alpha(T)$ in eq. (2) for both phases. For the temperature range

Table 1: Employed physical and numerical parameters for the simulations.

parameter	simulation value	physical value
Numerical parameters		
grid spacing Δx	1	$1 \times 10^{-6}\,\mathrm{m}$
time step Δt	0.025	$2.5 \times 10^{-4}\,\mathrm{s}$
interface width W	$2.5 \cdot 5 \cdot \Delta x$	$12.5 \times 10^{-6}\,\mathrm{m}$
Physical parameters		
surface energy $\gamma_{\alpha\beta}$	0.097879	$0.03\,\mathrm{J/m^2}$
diffusivity in suspension	1	$1 \times 10^{-10}\,\mathrm{m^2/s}$
diffusivity in ice	1×10^{-3}	$1 \times 10^{-13}\,\mathrm{m^2/s}$
kinetic coefficient $\tau_{\alpha\beta}$	33	$1.01\,\mathrm{Js/m^4}$
melting temperature T_m	1	$273.15\,\mathrm{K}$

of interest, the equilibrium conditions

$$G_s(c_s, T) + \mu_s(c_s, T)(c_i - c_s) - G_i(c_i, T) = 0 \tag{12}$$

$$\mu_s(c_s, T) - \mu_i(c_i, T) = 0 \tag{13}$$

are evaluated on the liquidus curve points (c_s, T) and the solidus curve points (c_i, T) for the suspension phase's Gibbs energy G_s and the ice phase's Gibbs energy G_i respectively. This yields a matrix of squared residuals whose minimization gives the functions $G_s(c, T), G_i(c, T)$ which generate a phase diagram with the minimal distance from the given phase boundaries. Again the `LSSolve` function of Maple is employed, this time with an additional constraint that the curvatures of the Gibbs energy curves are to be positive for the employed temperature ranges. The solid ice phase is assumed to be largely stoichiometric, with its solidus curve given by $c_i = (T_m - \frac{T}{5})/100$ in non-dimensional temperature T and melting temperature T_m. This slight dependence of the ice composition on the temperature is included for numerical stability.

This procedure can be executed for any desired particle radius, yielding Gibbs energy curves approximating a binary phase diagram according to the

theory of Peppin et al. In contrast, the prior work of Huang [11] does not consider the particle size at any time during model formulation or parametrization. Three particle radii r (250 nm, 375 nm and 500 nm) are studied in this paper, with the free energy parameters of each tabulated in the employed precision in the Supplementary Material. The resulting phase diagrams for all particle sizes are shown in one plot in fig. 1. As the solidus curve does not differ much between the particle sizes, only a single one was drawn. Generally the liquidus curve becomes flatter and moves towards the RDP with increasing particle size.

Furthermore, table 1 shows the remaining numerical and physical parameters necessary to conduct the simulation. The parameters were nondimensionalized by choosing the length scale $l_0 = 1\,\mu\text{m}$, the diffusion scale $D_0 = 1 \times 10^{-10}\,\text{m}^2/\text{s}$, the temperature scale $T_0 = 273.15\,\text{K}$, the energy density scale $E_0 = 3.065 \times 10^5\,\text{J/m}^3$ and the molar volume scale $V_{m,0} = 2 \times 10^{-5}\,\text{m}^3/\text{mol}$. Based on these the remaining scales of time, surface energy and kinetic coefficient can be derived. For each physical parameter, its dimensionless value is determined by dividing it by its corresponding scaling parameter.

4. Simulation conditions

The simulations are conducted as follows: A planar ice front is put in the left part of the domain and the rest of the domain is filled with the suspension at the investigated solids loading c_0. Periodic boundary conditions are applied on the top and bottom sides, whereas zero flux conditions are applied on the left (solid) side. On the right (liquid) side of the domain the phase-field has zero flux conditions and the solids loading is fixed to c_0 with a Dirichlet boundary condition. A moving window technique is applied in order to simulate a quasi-infinite domain in the growth direction. The planar ice front is set such that this moving window starts immediately. A graphical overview of the simulation setup can be seen in fig. 2a. Within this and following figures, yellow indicates the ice crystal and blue the suspension with the red-orange part indicating the diffuse interface. Additionally in fig. 2b the considered microstructural lengths

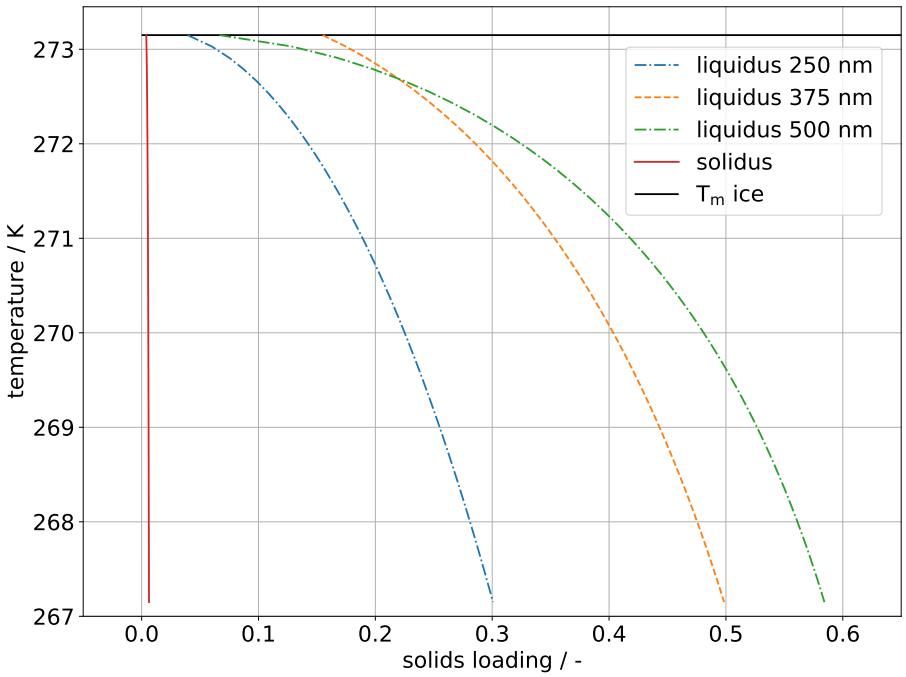

Figure 1: Back-calculated phase diagrams of freeze casting for three different particle sizes with the parameters from the Supplementary Material. Since the solidus curves are very close together only a single line is drawn. However, the liquidus curves differ significantly for each particle size. The larger the particle radius, the flatter the liquidus curve becomes.

are shown: The tip distance, or wavelength, λ, the ice trunk diameter d_{ice} and the suspension channel diameter d_{sus}. For the trunk and channel diameters the straight regions of pure ice and pure suspension are determined. Hence the region of side branches is excluded from the measurement which leads to $\lambda > d_{ice} + d_{sus}$.

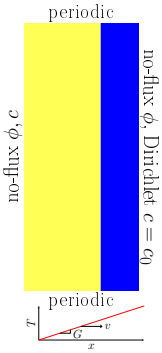

(a) Simulation setup for the directional solidification of the suspension.

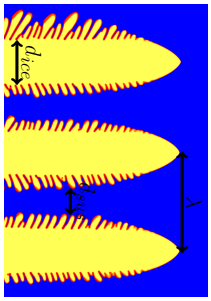

(b) Exemplary part of a steady-state simulation. λ is the tip distance, d_{ice} the ice trunk diameter and d_{sus} the suspension channel diameter.

Figure 2: Initial and boundary conditions of the simulation as well a subregion of an exemplary steady-state simulation. Yellow indicates the ice crystal and blue the suspension, with the red-orange part being the diffuse interface.

5. Results

Simulations are conducted with the following solidification conditions: Solids loading $c_0 \in \{0.075, 0.1, 0.15\}$, pulling velocity $v \in \{3.2, 6.4, 12.8\}$µm/s and temperature gradient $G \in \{1.5, 24\}$K/mm for the parameter sets for 250 nm, 375 nm as well as 500 nm particle suspensions, resulting in 54 simulations. The first temperature gradient is similar to the one found in experiments [31] with the second one chosen for quicker convergence of the microstructure. The simulations are continued until no dendrite is moving significantly out of the moving window. Figure 3 gives an overview of the final simulated microstructure for various parameters. Several observations are evident: The microstructure is refined by

higher pulling velocities v and dendritic side branches are less developed. The latter effect is likely caused by the distance between dendritic trunks decreasing which causes diffusion-mediated suppression of the side branches. In contrast the solids loading directly changes the mass fraction of ice to suspension, with an increase of the solids loading causing a widening of the suspension channels and a narrowing of the ice trunks. Furthermore, dendritic side branches become more prominent for higher solids loading as the trunk distance grows. Finally, increasing the particle size generally lessens side branching by decreasing the trunk distance. Simulation snapshots of all conducted simulations in their final state are available in the Supplementary Material.

6. Discussion

The tip distance λ, the ice trunk diameter d_{ice} and the suspension channel diameter d_{sus} are measured as the microstructural length parameters in each simulation. In order to build a relationship between the processing parameter set $\{c_0, v, G\}$ and the output microstructural length, it is assumed that a power law relationship holds for each parameter and that the parameters' effect can be separated, i.e. their product yields the microstructural length up to a constant multiplier. Hence the results will be fitted to the model

$$L = Ac_0^n v^m G^o \tag{14}$$

with L being any of the microstructural lengths. This model is similar to analytical models for dendritic growth in alloy solidification [32], except that the solids loading c_0 takes the place of the solidification range ΔT_0. In the following, the model is fitted to the different simulated microstructural lengths and the results discussed. The main thrust of this discussion will be on the scaling laws and hence the prefactor A will not be discussed, but reported for completeness' sake. Table 2 provides an overview of the predicted, observed and fitted results for scaling laws from literature as well as this work. In the following, the fitting results will be discussed and compared to theoretical and experimental results.

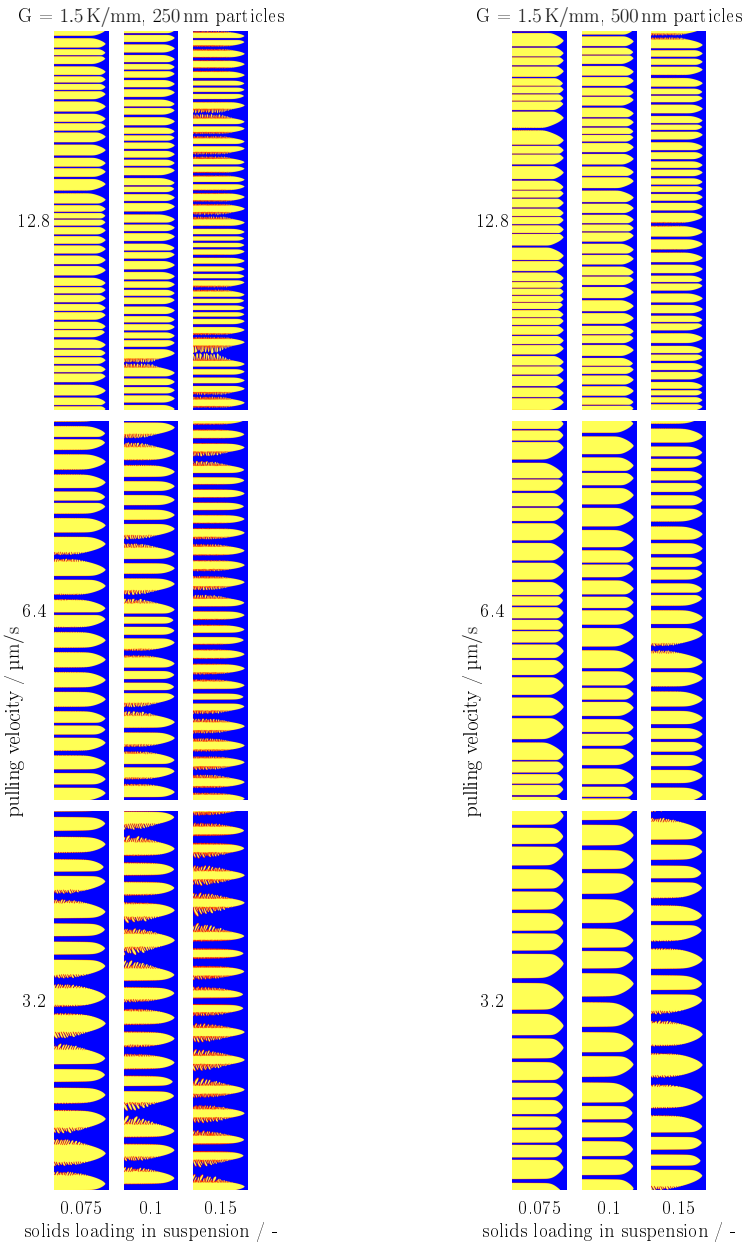

Figure 3: Overview of simulation results for suspensions of 250 nm and 500 nm particles being directionally solidified in a 1.5 K/mm temperature gradient. Increasing the pulling velocity refines the structure in general. Increasing the solids loading roughens the side structure of the ice dendrite and decreases the fraction of ice trunk diameter to suspension channel diameter. Freeze-cast suspensions with larger particles tend to show less dendritic features.

Table 2: Predicted, observed and fitted parameters to eq. (14).

L predicted/fitted/observed	n in c_0^n	m in v^m	o in G^o
λ predicted by Kurz et al. [32]	-	-0.5 (cells), -0.25 (dendrites)	-0.5
λ observed by Waschkies et al. [31]	-	-0.8 to -1.3	-
λ observed by Deville et al. [33]	-	-0.67 to -1	-
λ fitted in this work, 250 nm particles	-0.07088 ± 0.06306	-0.6058 ± 0.03714	-0.2675 ± 0.01658
λ fitted in this work, 375 nm particles	$+0.04561 \pm 0.03953$	-0.5699 ± 0.02304	-0.2317 ± 0.009860
λ fitted in this work, 500 nm particles	$+0.08709 \pm 0.04294$	-0.5847 ± 0.02525	-0.2037 ± 0.01029
d_{sus} fitted in this work, 250 nm particles	$+0.3733 \pm 0.1037$	-0.6995 ± 0.06473	-0.4193 ± 0.03747
d_{sus} fitted in this work, 375 nm particles	$+0.5611 \pm 0.05328$	-0.7520 ± 0.03389	-0.1699 ± 0.01207
d_{sus} fitted in this work, 500 nm particles	$+0.6485 \pm 0.09631$	-0.7754 ± 0.06159	-0.05052 ± 0.01963
d_{ice} fitted in this work, 250 nm particles	-0.7147 ± 0.09337	-0.3119 ± 0.04442	-0.1488 ± 0.01882
d_{ice} fitted in this work, 375 nm particles	-0.4091 ± 0.07633	-0.4488 ± 0.04028	-0.2590 ± 0.01902
d_{ice} fitted in this work, 500 nm particles	-0.1987 ± 0.05944	-0.3877 ± 0.03151	-0.2134 ± 0.01415

First, the results for particles of 250 nm radius are used for parametrizing this model. Fitting the simulation data for the wavelength λ against this model yields the parameters plus-minus the standard deviation $A = 4729\,\mu\text{m} \pm 956.0\,\mu\text{m}$, $n = -0.07088 \pm 0.06306$, $m = -0.6058 \pm 0.03714$, $o = -0.2675 \pm 0.01658$, with v in µm/s and G in K/m. The velocity exponent m is close to the range of experimentally reported values $[-0.67, -1.3]$[31, 33, 34]. Note that as [33] mentions the velocity exponent depends on the particle size, the effect of which will be shown shortly. However, none of the experimental studies systematically studied the influence of the temperature gradient on the structural wavelength. The aforementioned model by Kurz et al. [32] predicts an exponent of -0.5, whereas here a temperature gradient exponent o of roughly half this value is observed. While this difference remains to be investigated, it does imply that care should be taken to control the temperature gradient during freeze casting, as it has a significant influence on the wavelength of the microstructure. The exponent n for the solids loading c_0 is harder to compare with existing models as these typically employ the solidification range ΔT_0. However, drawing a scatter plot of the solids loading and the observed wavelength for several velocities, as shown in fig. 4, helps to interpret the result: The wavelength is mainly determined by the pulling velocity v and the temperature gradient G, with the solids loading showing only a minor effect. The direction of this effect even changes for the higher gradient, hence the small value for n and its comparably large standard deviation can be interpreted as the solids loading having close to no correlation to the structural wavelength for this particle size.

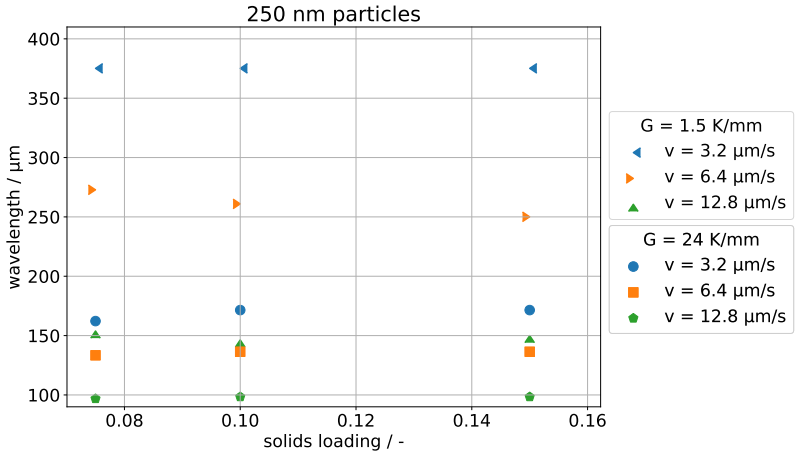

Figure 4: Scatter plot of the solids loading and observed wavelength with 250 nm particles. The triangular symbols indicate the observations for $G = 1.5\,\mathrm{K/mm}$ and the rest for $G = 24\,\mathrm{K/mm}$. The solids loading only has a minor effect on the observed wavelength compared to the pulling velocity and temperature gradient. Furthermore, its effect apparently reverses direction for the higher gradient.

Fitting the model with measured suspension channel diameter d_{sus} yields the parameters $A = 10.48\,\mathrm{mm} \pm 3.953\,\mathrm{mm}$, $n = 0.3733 \pm 0.10364$, $m = -0.6995 \pm 0.06473$, $o = -0.4193 \pm 0.03747$. The velocity exponent now crosses into the range of experimentally observed exponents and the temperature gradient exponent is closer to the model by Kurz et al. [32]. However, the exponent for the solids loading has changed appreciably. In order to interpret this, consider that the suspension channels are closely related to the dense part of the structure after the freeze-casting process is finished. The density, or equivalently porosity, has been experimentally shown [34] to depend linearly on the solids loading of the suspension, which would correspond to a solids loading exponent of $n = 1$ for the dense part of the structure. However, the suspension channels in the simulation do not correspond exactly to the solid walls within the freeze-cast structure, as the solidification is not finished and the channel diameter disregards the ambiguous region of side branches. Furthermore, the suspension channel diameter itself is modulated by the wavelength λ. In order

to show the linear relationship between density and solids loading, the observed mass fraction of the suspension below the dendrite tips is plotted over the solids loading in fig. 5 along with a linear fit to the data for a velocity of 12.8 μm/s. The fit is also calculated for the remaining velocites and gradients, all of which show good correlation ($R^2 \geq 0.995$), suggesting that the model reproduces the linear relationship between solids loading and density as found in experiments.

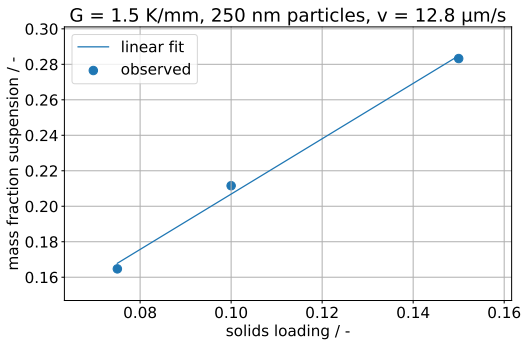

Figure 5: The mass fraction of the suspension below the dendrite tips vs solids loading for $\{G = 1.5\,\mathrm{K/mm}, v = 12.8\,\mu\mathrm{m/s}\}$ with 250 nm particles.

Finally, applying the model to the ice dendrite trunk diameter d_{ice} yields the parameters $A = 148.5\,\mu\mathrm{m} \pm 41.61\,\mu\mathrm{m}$, $n = -0.7147 \pm 0.09337$, $m = -0.3119 \pm 0.04442$, $o = -0.1488 \pm 0.01881$. These are very different from the previous results and indicate that the ice trunk diameter is less sensitive to changes in the gradient and the solidification velocity but more sensitive to changes in the solids loading compared to the suspension channel diameter. The sign change of the solids loading exponent directly follows from the ice phase rejecting particles and hence when more particles are present, less space is available for the ice to solidify. Calculating the mass fraction of ice as above also indicates that a linear relationship, now with negative slope, exists between the ice mass fraction and the solids loading of the suspension.

Next, the simulation results for particles of 375 nm radius are used for parametrizing eq. (14). The fitting parameters $A = 4471\,\mu\mathrm{m} \pm 555.0\,\mu\mathrm{m}$, $n =$

0.04561 ± 0.03953, $m = -0.5699 \pm 0.02304$, $o = -0.2317 \pm 0.009862$ are obtained for the wavelength λ. In contrast to the 250 nm particle results, the concentration exponent n is now positive. Furthermore its standard deviation relative to the exponent is smaller, which suggests that there is a small coarsening effect on the wavelength when increasing the solids loading. The corresponding scatter plot in fig. 6 shows mostly irregular behavior again but with more points trending upwards for higher solids loading. Both the velocity exponent m and the temperature gradient exponents o have decreased slightly from the previous case.

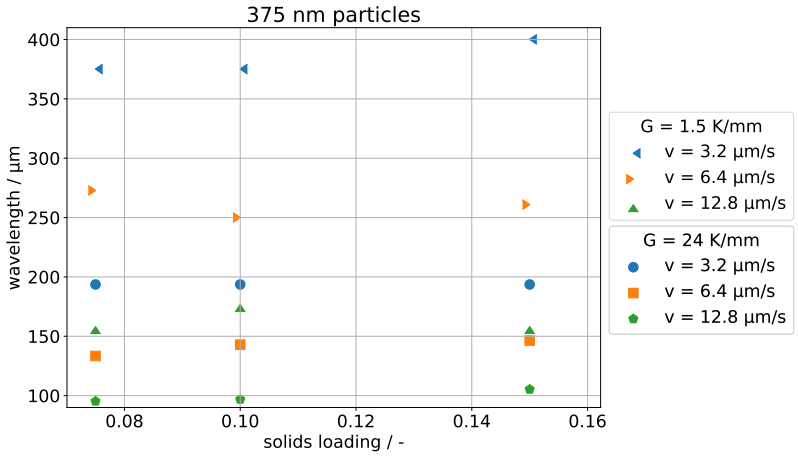

Figure 6: Scatter plot of the solids loading and observed wavelength with 375 nm particles. The triangular symbols indicate the observations for $G = 1.5\,\mathrm{K/mm}$ and the rest for $G = 24\,\mathrm{K/mm}$. The effect of the solids loading on the wavelength is still minor compared to the pulling velocity and temperature gradient. However more points tend to trend upwards with a higher solids loading.

Fitting the data for the suspension channel diameter d_{sus} yields $A = 2387\,\mu\mathrm{m} \pm 381.6\,\mu\mathrm{m}$, $n = 0.5611 \pm 0.05328$, $m = -0.7520 \pm 0.03389$, $o = -0.1699 \pm 0.01207$. The solids loading exponent is now closer to the expected value of 1. As can be seen in fig. 1, for a given undercooling below the liquidus, the suspensions with larger particles will have an equilibrium solids loading closer to the random dense-packing density of 0.64. The liquidus becomes very steep close to

this RDP, similar to the stoichiometric solidus line. Hence a suspension region which achieves this concentration range will stay close to it, even if it is cooled down further. In combination with the stoichiometric solidus line this implies that a constant partition coefficient $k = x_i/x_s$ with the equilibrium solids loading in the ice x_i and the suspension x_s is achieved. Away from this region the partition coefficient is a function of temperature. Thus it is likely that more cells in the growth direction below the moving window point would further move the solids loading exponent to a value of 1, as a bigger part of the simulation domain would have an almost constant partition coefficient. The velocity exponent m increased from the 250 nm particle results whereas the temperature gradient exponent o decreased.

Employing the data for the ice trunk diameter d_{ice} yields $A = 1167\,\mu\text{m} \pm 281.9\,\mu\text{m}$, $n = -0.4091 \pm 0.07633$, $m = -0.4488 \pm 0.04028$, $o = -0.2590 \pm 0.01902$. As with the suspension channel results, the velocity exponent shows a slight increase. Contrary to those results, the temperature gradient exponent o increased. The solids loading exponent is still negative but has decreased substantially.

Finally, the simulations results for particles of 500 nm radius are used for parametrizing eq. (14). For the structural wavelength λ, the parameters $A = 3791\,\mu\text{m} \pm 504.5\,\mu\text{m}$, $n = 0.08709 \pm 0.04294$, $m = -0.5847 \pm 0.02525$, $o = -0.2037 \pm 0.01029$ are obtained. As with the 375 nm results, a slight coarsening effect of increased solids loading is present, with even more points trending upwards in a scatter plot. The effect of the temperature gradient on the wavelength seems to decrease slightly with increasing particle size. The velocity exponent is close to that of 375 nm particle suspensions, though slightly larger now. In [33] the authors observed a velocity exponent of 1 for 400 nm particles and one of $\frac{2}{3}$ for 100 nm particles, both suspended in water. The present study shows a minor effect in the other direction, that is the velocity exponent increases as the particle size is reduced. However, the magnitude of this effect relative to the error in the exponent does not suggest that the effect is significant. An explanation for the dependence of the velocity exponent is the concentration and

particle size dependent diffusivity [35]. However, the present study assumes a constant diffusivity of particles in the suspension. Hence the variation of the velocity exponent is likely to be largely a function of the kinetics represented by diffusivity, with only minor energetic influences.

For the suspension channel diameter d_{sus} the parameters $A = 965.7\,\mu\text{m} \pm 272.5\,\mu\text{m}$, $n = 0.6485 \pm 0.09631$, $m = -0.7754 \pm 0.06159$, $o = -0.05052 \pm 0.01963$ are obtained. The velocity exponent is now higher than for the suspension with smaller particles, but the ranges including the error overlap again. The trend of increasing solids loading exponent with increasing particle size continues, although in a less significant way as the ranges including the error overlap now. Furthermore, the dependence of the suspension channel diameter on the temperature gradient is significantly smaller than for the suspensions with smaller particles. Scatter plots of the suspension channel diameter against the temperature gradient generally show a refinement effect, with two outliers. One shows almost no refinement and the other a coarsening effect on the suspension channel, whereas both the wavelength and ice trunk exhibit refinement. Excluding those two outliers roughly doubles the exponent, but even at -0.1 there is still a significant difference to the results for suspension with smaller particle sizes which remains to be investigated further.

Lastly, fitting against the results for the ice trunk diameter d_{ice} yields the parameters $A = 1122\,\mu\text{m} \pm 207.6\,\mu\text{m}$, $n = -0.1987 \pm 0.05944$, $m = -0.3878 \pm 0.03151$, $o = -0.2134 \pm 0.01415$. The solids loading exponent has become even smaller at this particle size, continuing the trend of previous particle size variations. In contrast, both the velocity and temperature gradient do not follow the previous trends.

7. Conclusions and outlook

A new parametrization of the freeze-casting process with the phase-field grand potential approach was presented. Within this, the complex capillary and kinetic anisotropy of the ice-water interface was qualitatively approximated

with sums of spherical harmonics. The as-of-yet experimentally undetermined thermodynamics of an aqueous colloidal suspension were approximated by relying on a previously calculated phase boundary by Peppin et al. [13, 30]. Based on these approximations, simulations in the dendritic morphology regime were conducted for suspensions with particles of radius 250 nm, 375 nm and 500 nm. The wavelength, the suspension channel diameter and the ice trunk diameter were measured in the steady-state regime and connected to the input processing parameters of velocity, temperature gradient and solids loading of the suspension. Qualitatively, observations showed that higher velocities and temperature gradients refined the microstructure for all three considered microstructural lengths. Increasing the solids loading yielded larger suspension channels and narrower ice trunks with the dendritic features becoming less prominent. A simple power law model was fitted to the simulated data in order to determine scaling relationships between the processing parameters and the microstructural lengths.

The wavelength was shown to depend mostly on the pulling velocity and the temperature gradient, with an increase of either leading to a smaller wavelength. This suggests that temperature gradients should be controlled in experiments in order to make them more comparable. In contrast to e.g. [33], an increase in particle size in the results shows a small reduction of the velocity exponent. Since in this study only the energetic and not the kinetic effects of changing the particle size was considered, the experimental behavior is likely to be largely attributable to kinetic effects such as the concentration and particle size dependent diffusivity. There was little influence of the solids loading on the wavelength for the smallest particle size. For the two bigger particle sizes, increasing the solids loading slightly increased the wavelength.

The suspension channel diameter, which roughly corresponds to the width of the solid walls within the final freeze-cast structure, showed a bigger dependence on the employed pulling velocity with the exponent also being closer to the experimentally observed range. This dependence slightly grew with increasing particle size similar to [33]. While an increase of the temperature gradient also

led to smaller suspension channel diameters, the magnitude of the influence seems to strongly depend on the particle size. At the largest investigated particle size, the influence of the temperature gradient was minor compared to both the pulling velocity and solids loading. An increase in the solids loading showed larger suspension channel diameters with its exponent getting larger and closer to 1 with increasing particle size. It was shown that the mass fraction of the suspension phase below the dendrite tips is a linear function of the solids loading with positive slope, as is commonly found in experiments.

Finally, the ice trunk diameter, which roughly corresponds to the pore width within the final freeze-cast structure, showed a smaller dependence on the employed pulling velocity. The magnitude of the pulling velocity dependence changed with the particle size but without an obvious trend. Similar results are found for the temperature gradient. An increase in solids loading showed smaller ice trunk diameters with its dependence becoming smaller for larger particles.

In total the results suggest that coarse-graining the individual particles into a concentration field is a viable approach for simulating freeze-casting. A future study investigating the effect of concentration and particle size dependent diffusivity should be conducted in order to test whether this kinetic effect reproduces the experimentally observed dependence of the velocity scaling law on the particle size.

8. Acknowledgements

The authors are grateful for funding the research work through the DFG project “Untersuchungen zur modellmäßigen Beschreibung und Vorhersage der Gefügeausbildung beim Gefriergießen” (grant number NE822/9-2). The authors gratefully acknowledge the Gauss Centre for Supercomputing e.V. (www.gauss-centre.eu) for funding this project by providing computing time on the GCS Supercomputer HAWK at Höchstleistungsrechenzentrum Stuttgart (www.hlrs.de).

Data availability

The raw/processed data required to reproduce these findings cannot be shared at this time as the data also forms part of an ongoing study.

Declaration of Competing Interest

The authors declare that they have no known competing financial interests or personal relationships that could have appeared to influence the work reported in this paper.

References

[1] S. W. Sofie, F. Dogan, Freeze Casting of Aqueous Alumina Slurries with Glycerol, Journal of the American Ceramic Society 84 (2001) 1459–1464.

[2] Y. Liu, W. Zhu, K. Guan, C. Peng, J. Wu, Freeze-casting of alumina ultrafiltration membranes with good performance for anionic dye separation, Ceramics International 44 (2018) 11901 – 11904.

[3] H. Schoof, J. Apel, I. Heschel, G. Rau, Control of pore structure and size in freeze-dried collagen sponges, Journal of Biomedical Materials Research 58 (2001) 352–357.

[4] S. Deville, E. Saiz, A. P. Tomsia, Freeze casting of hydroxyapatite scaffolds for bone tissue engineering, Biomaterials 27 (2006) 5480–5489.

[5] U. G. K. Wegst, M. Schecter, A. E. Donius, P. M. Hunger, Biomaterials by freeze casting, Philosophical Transactions of the Royal Society A: Mathematical, Physical and Engineering Sciences 368 (2010) 2099–2121.

[6] S. Deville, Ice-templating, freeze casting: Beyond materials processing, Journal of Materials Research 28 (2013) 2202–2219.

[7] G. Liu, Fabrication of porous ceramics and composites by a novel freeze casting process, Measurement (2011) 247.

[8] A. Karma, W.-J. Rappel, Quantitative phase-field modeling of dendritic growth in two and three dimensions, Physical Review E 57 (1998) 4323–4349.

[9] A. Karma, Phase-field formulation for quantitative modeling of alloy solidification, Physical Review Letters 87 (2001) 115701–1–115701–4.

[10] R. Folch, M. Plapp, Quantitative phase-field modeling of two-phase growth, Physical Review E 72 (2005) 011602.

[11] T. H. Huang, T. H. Huang, Y. S. Lin, C. H. Chang, P. Y. Chen, S. W. Chang, C. S. Chen, Phase-Field Modeling of Microstructural Evolution by Freeze-Casting, Advanced Engineering Materials 20 (2018) 1–13.

[12] B. Echebarria, R. Folch, A. Karma, M. Plapp, Quantitative Phase Field Model of Alloy Solidification, Physical Review E 70 (2004) 1–51.

[13] S. S. Peppin, J. A. Elliott, M. G. Worster, Solidification of colloidal suspensions, Journal of Fluid Mechanics 554 (2006) 147–166.

[14] A. Choudhury, B. Nestler, Grand-potential formulation for multicomponent phase transformations combined with thin-interface asymptotics of the double-obstacle potential, Phys. Rev. E 85 (2012) 021602.

[15] M. Plapp, Unified derivation of phase-field models for alloy solidification from a grand-potential functional, Phys. Rev. E 84 (2011) 031601.

[16] N. Moelans, A quantitative and thermodynamically consistent phase-field interpolation function for multi-phase systems , Acta Materialia 59 (2011) 1077–1086.

[17] J. Langer, in: C. Godreche (Ed.), Solids far from equilibrium, Edition Alea Saclay, Cambridge, UK, 1991, p. 297.

[18] J. Hötzer, A. Reiter, H. Hierl, P. Steinmetz, M. Selzer, B. Nestler, The parallel multi-physics phase-field framework pace3d, Journal of computational science 26 (2018) 1–12.

[19] S. R. Coriell, S. C. Hardy, R. F. Sekerka, A non-linear analysis of experiments on the morphological stability of ice cylinders freezing from aqueous solutions, Journal of Crystal Growth 11 (1971) 53–67.

[20] D. R. H. Jones, The measurement of solid-liquid interfacial energies from the shapes of grain-boundary grooves, The Philosophical Magazine: A Journal of Theoretical Experimental and Applied Physics 27 (1973) 569–584.

[21] S. C. Hardy, A grain boundary groove measurement of the surface tension between ice and water, Philosophical Magazine 35 (1977).

[22] L. Gránásy, T. Pusztai, P. F. James, Interfacial properties deduced from nucleation experiments: A Cahn-Hilliard analysis, Journal of Chemical Physics 117 (2002).

[23] T. Kuroda, R. Lacmann, GROWTH KINETICS OF ICE FROM THE VAPOUR PHASE AND ITS GROWTH FORMS, Journal of Crystal Growth 56 (1982) 189–205.

[24] R. Handel, R. L. Davidchack, J. Anwar, A. Brukhno, Direct Calculation of Solid-Liquid Interfacial Free Energy for Molecular Systems : TIP4P Ice-Water Interface, Physical review letters 036104 (2008) 1–4.

[25] R. L. Davidchack, R. Handel, J. Anwar, A. V. Brukhno, Ice Ih-Water Interfacial Free Energy of Simple Water Models with Full Electrostatic Interactions, Journal of Chemical Theory and Computation (2012).

[26] P. V. Hobbs, Ice physics, Oxford university press, 1973.

[27] M. Maruyama, Y. Kishimoto, T. Sawada, Optical study of roughening transition on ice I h (1010) planes, Journal of Crystal Growth 172 (1997) 521–527.

[28] K. Nagashima, Y. Furukawa, Nonequilibrium effect of anisotropic interface kinetics on the directional growth of ice crystals, Journal of Crystal Growth 171 (1997) 577–585.

[29] R. Feistel, W. Wagner, A New Equation of State for Ice Ih A New Equation of State for H2O Ice Ih, Journal of Physical and Chemical Reference Data 1021 (2006).

[30] S. S. L. Peppin, J. S. Wettlaufer, M. G. Worster, Experimental verification of morphological instability in freezing aqueous colloidal suspensions, Physical Review Letters 100 (2008) 1–4.

[31] T. Waschkies, R. Oberacker, M. J. Hoffmann, Investigation of structure formation during freeze-casting from very slow to very fast solidification velocities, Acta Materialia 59 (2011) 5135–5145.

[32] W. Kurz, D. J. Fisher, Dendrite growth at the limit of stability: tip radius and spacing, Acta Metallurgica 29 (1981) 11–20.

[33] S. Deville, E. Saiz, A. P. Tomsia, Ice-templated porous alumina structures, Acta Materialia 55 (2007) 1965–1974.

[34] S. Deville, Freeze-casting of porous ceramics: A review of current achievements and issues, Advanced Engineering Materials 10 (2008) 155–169.

[35] S. Flauder, U. Gbureck, F. A. Müller, Structure and mechanical properties of β-TCP scaffolds prepared by ice-templating with preset ice front velocities, Acta Biomaterialia 10 (2014) 5148–5155.

Supplementary material to Modelling and simulation of the freeze casting process with the phase-field method

Marco Seiz, Britta Nestler

February 15, 2021

1 Gibbs free energy parameters

This section details the numerical values employed to describe the Gibbs free energy of aqueous bentonite suspensions with particles of size 250 nm, 375 nm and 500 nm. All values are nondimensionalized based on the scales noted in the main text, with $G_{dim} = G \cdot E_0$. For each particle size, the Gibbs free energy of both the solid ice phase $G_i(c,T)$ and the liquid suspension phase $G_s(c,T)$ are reported. Both are of the form

$$G_\alpha(c,T) = A_\alpha(T)c^2 + B_\alpha(T)c + C_\alpha(T)$$

with $A_\alpha(T), B_\alpha(T), C_\alpha(T)$ being parabolic functions of temperature T. The functions $C_i(T), C_s(T)$ for the ice and suspension phases are independent of the particle size since they are based on the pure phase description following IAPWS.

Table 1: particle size independent functions

$C_i(T)$	$-843.987154950033T^2 + 2668.14452736135T - 1823.8679855496$
$C_s(T)$	$-1862.28940047943T^2 + 3718.19539783286T - 1855.56475865368$

The functions $A_\alpha(T), B_\alpha(T)$ for the ice and suspensions phases are tabulated below for each particle size:

Table 2: functions for 250 nm particles

$A_i(T)$	$-363.8130527019557^2 + 1038.42737506969 * T - 661.07371316661$
$A_s(T)$	$+624.781729505937T^2 - 2001.5373528048 * T + 1603.02054720731$
$B_i(T)$	$-14305.5893356235T^2 + 26721.0370280905 * T - 12534.9375540961$
$B_s(T)$	$-363.8130527019557^2 + 1038.42737506969 * T - 661.07371316661$

Table 3: functions for 375 nm particles

$A_i(T)$	$8696450.19594392T^2 - 16499259.5809074T + 7827020.0745525$
$A_s(T)$	$+4419.53212429992T^2 - 9890.27278224592T + 5533.24950362982$
$B_i(T)$	$-130214.073750852T^2 + 245337.628150446T - 115442.978896433$
$B_s(T)$	$12514.870762504T^2 - 23252.2358392643T + 10773.1205717657$

Table 4: functions for 500 nm particles

$A_i(T)$	$+995906.442526578T^2 - 2106381.19059346T + 1113015.48143482$
$A_s(T)$	$+10047.1312993791T^2 - 21246.3527768701T + 11224.7417646649$
$B_i(T)$	$-5645.19688672837T^2 + 11679.3939071022T - 6046.24602532013$
$B_s(T)$	$+2941.69029612794T^2 - 5300.34949864201T + 2371.22834220704$

Finally, the full Gibbs energy functions for the different particle sizes are also given:

$$\begin{aligned} G_{i,250\,\mathrm{nm}} =&(750591.374527449 * T^2 - 1.47463039577804 * 10^6 * T + 743122.943915487) * c^2 \\ &+ (-14305.5893356235 * T^2 + 26721.0370280905 * T - 12534.9375540961) * c \\ &- 843.987154950033 * T^2 + 2668.14452736135 * T - 1823.8679855496 \end{aligned}$$

$$\begin{aligned} G_{s,250\,\mathrm{nm}} =&(1603.02054720731 - 2001.5373528048 * T + 624.781729505937 * T^2) * c^2 \\ &+ (-363.813052701955 * T^2 + 1038.42737506969 * T - 661.07371316661) * c \\ &- 1862.28940047943 * T^2 + 3718.19539783286 * T - 1855.56475865368 \end{aligned}$$

$$\begin{aligned} G_{i,375\,\mathrm{nm}} =&(8.69645019594392 * 10^6 * T^2 - 1.64992595809074 * 10^7 * T + 7.82702007455250 * 10^6) * c^2 \\ &+ (-130214.073750852 * T^2 + 245337.628150446 * T - 115442.978896433) * c \\ &- 843.987154950033 * T^2 + 2668.14452736135 * T - 1823.86798554960 \end{aligned}$$

$$\begin{aligned} G_{s,375\,\mathrm{nm}} =&(5533.24950362982 - 9890.27278224592 * T + 4419.53212429992 * T^2) * c^2 \\ &+ (12514.8707625040 * T^2 - 23252.2358392643 * T + 10773.1205717657) * c \\ &- 1862.28940047943 * T^2 + 3718.19539783286 * T - 1855.56475865368 \end{aligned}$$

$$\begin{aligned} G_{i,500\,\mathrm{nm}} =&(703345.204001284 * T^2 - 1.51219218860276 * 10^6 * T + 812645.048703083) * c^2 \\ &+ (-6458.38650416161 * T^2 + 13153.8099858636 * T - 6713.44791450838) * c \\ &- 843.987154950033 * T^2 + 2668.14452736135 * T - 1823.86798554960 \end{aligned}$$

$$
\begin{aligned}
G_{s,500\,\mathrm{nm}} =& (7984.99647865678 - 14858.7003887071 * T + 6911.02343660797 * T^2) * c^2 \\
&+ (3754.87978653526 * T^2 - 6774.76533796470 * T + 3038.43011872479) * c \\
&- 1862.28940047943 * T^2 + 3718.19539783286 * T - 1855.56475865368
\end{aligned}
$$

2 Simulation snapshots

The following images show simulation snapshots of all conducted simulations in their final state. The field shown is the phase-field of the ice phase, with yellow indicating ice and blue indicating suspension. The red-orange part in between is the diffuse interface.

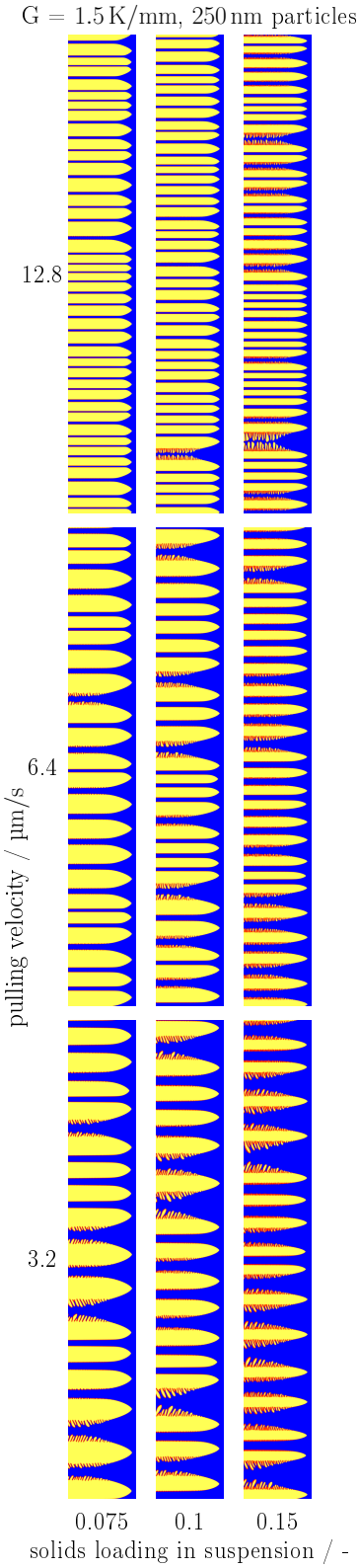
G = 1.5 K/mm, 250 nm particles
12.8
6.4
3.2
pulling velocity / µm/s
0.075
0.1
0.15
solids loading in suspension / -

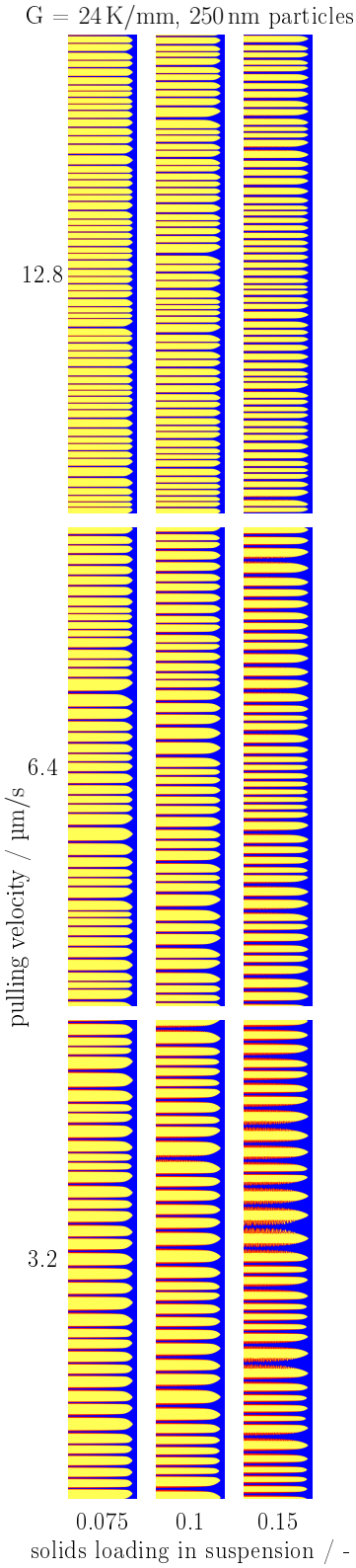
G = 24 K/mm, 250 nm particles
12.8
6.4
3.2
pulling velocity / µm/s
0.075
0.1
0.15
solids loading in suspension / -

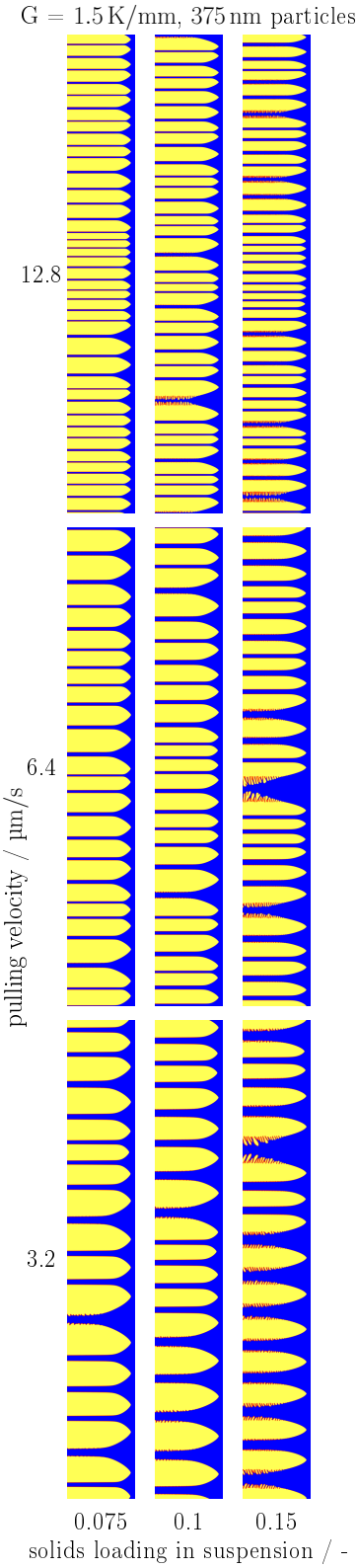
G = 1.5 K/mm, 375 nm particles
12.8
6.4
3.2
pulling velocity / µm/s
0.075
0.1
0.15
solids loading in suspension / -

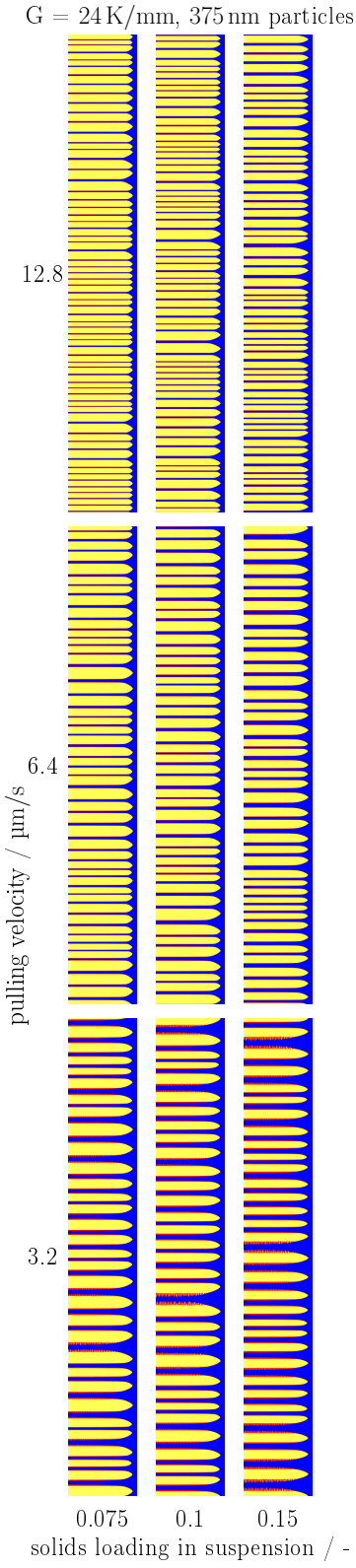
G = 24 K/mm, 375 nm particles
12.8
6.4
3.2
pulling velocity / µm/s
0.075
0.1
0.15
solids loading in suspension / -

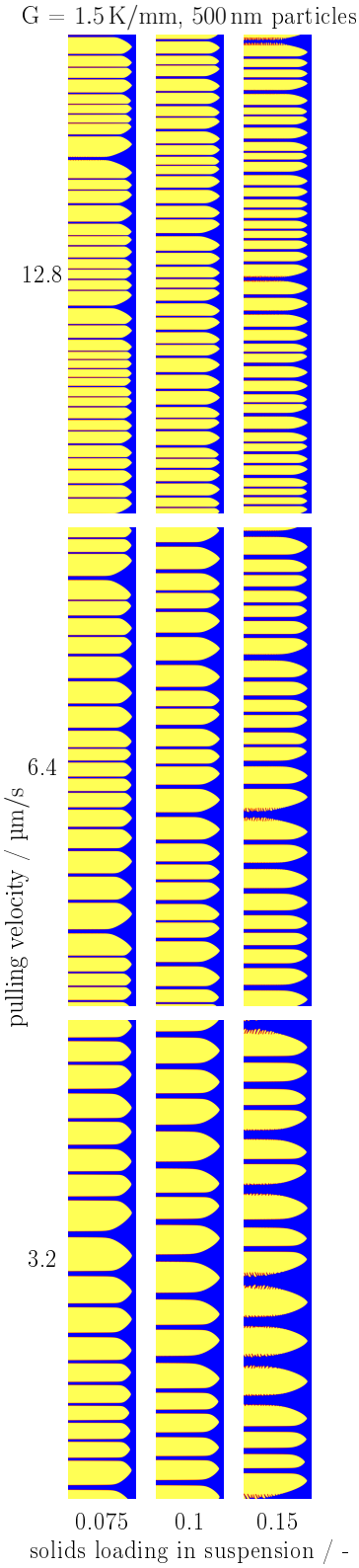
G = 1.5 K/mm, 500 nm particles
12.8
6.4
3.2
pulling velocity / µm/s
0.075
0.1
0.15
solids loading in suspension / -

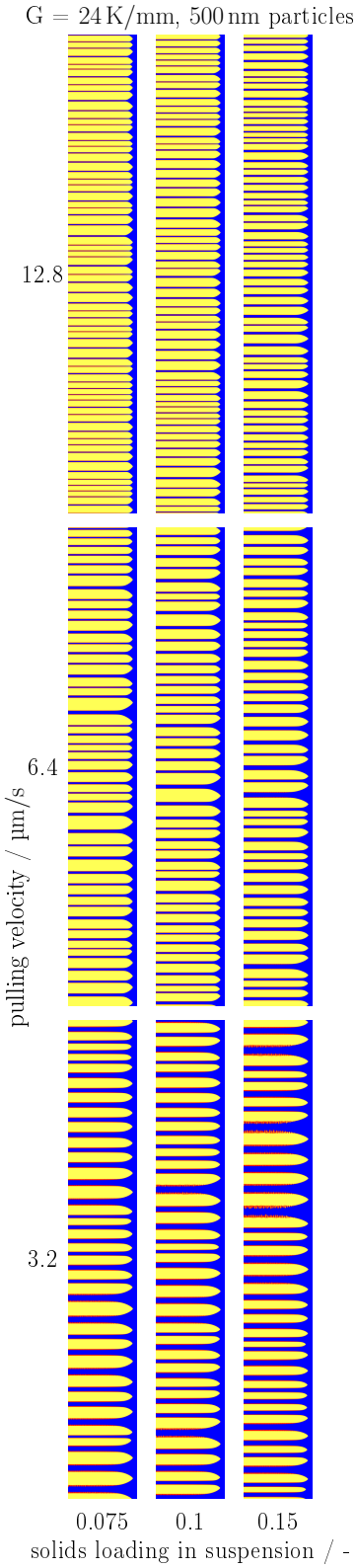
G = 24 K/mm, 500 nm particles
12.8
6.4
3.2
pulling velocity / µm/s
0.075
0.1
0.15
solids loading in suspension / -